Supplement of Atmos. Chem. Phys., 21, 14215–14234, 2021
https://doi.org/10.5194/acp-21-14215-2021-supplement

Atmospheric Chemistry and Physics
Open Access
EGU

Supplement of

Laboratory and field studies of ice-nucleating particles from open-lot livestock facilities in Texas

Naruki Hiranuma et al.

Correspondence to: Naruki Hiranuma (nhiranuma@wtamu.edu)

S1. Chemical composition analysis

Single-particle mass spectra of dry dispersed TXD particles in the size range between 200 and 2500 nm (vacuum aerodynamic diameter) were measured in the lab using a laser ablation aerosol particle time-of-flight mass spectrometer (LAAPTOF; AeroMegt GmbH) (Shen et al., 2018; 2019). The powder particles were generated by powder dispersion using a rotating brush generator (PALAS GmbH, RBG1000), where a small volume of dry samples was dispersed by dry synthetic air.

The averaged mass spectra of TXD01 and TXD05 are shown in **Fig. S1**. In general, the mass spectra of the dry dispersed particles showed high signals of organic markers at mass-to-charge ratio, m/z, of +44 ($COO/C_2H_6N^+$), -26 ($CN/C_2H_2^-$), -42 ($CNO/C_2H_2O^-$), -45 ($COOH^-$), -59 (CH_2COOH^-), -71 (CCH_2COOH^-), +30 ($NO/CH_3NH/CH_2O^+$), +58 (C_2H_5-NH-CH_2^+), and +59 ($(CH_3)_3N^+$). These are typical markers for organic acids and amine-containing particles. For example, peaks at m/z of +44 can be attributed to $COO/CH2NO^+$ derived from organic compounds/nitrogen-containing organic compounds (Schneider et al., 2011). It should be noted that m/z 44 can also be contributed by SiO^+, which is a silicon marker (Silva and Prather, 2000). Further, -45 ($COOH^-$), -59 (CH_2COOH^-), and -71 (CCH_2COOH^-) are the markers for carboxylic acids. The peak at m/z of +30 can be attributed to NO^+ arising from nitrate, ammonium (Murphy et al., 2006; Shen et al., 2018), and CH_3NH^+ from amines (Silva and Prather, 2000; Schmidt et al., 2017). The other amine markers at +58 ($C_2H_5NHCH_2^+$) and +59 ($(CH_3)_3N^+$) were identified by previous studies (e.g., Angelino et al., 2001; Pratt et al., 2009; Schmidt et al., 2017).

For the inorganic markers, the characteristic ions were found on the peaks at m/z +23 (Na^+), +24 (Mg^+), +27 (Al^+), +28 (Si^+), +39 (K^+), +40 (Ca^+), +44 (SiO^+), +56 (CaO/Fe^+), +64/66 (Zn^+), -97 (HSO_4^-),+30 (NO^+), -63 (PO_2^-), -79 (PO_3^-), and -95 (PO_4^-). Calcium and sodium are used as additives in the diet fed to the cattle, and they also exist in the unpaved road dust (National Research Council, 2000; Ocsay et al., 2006). Manure is a source of ammonium and phosphate. Minor fractions of other salts and mineral dust constituents found in this work were also identified in the field samples (Hiranuma et al., 2011 and references therein). As mentioned above, +30 NO^+ can arise from ammonium (Murphy et al., 2006; Shen et al., 2018). In addition, -63 (PO_2^-), -79 (PO_3^-), and -95 (PO_4^-) are phosphate markers (Schmidt et al., 2017; Zawadowicz et al., 2017). However, our inorganic quantification is inconclusive, and the result may deviate from other quantitative composition analyses.

Comparing TXD01 to TXD05, we found that TXD01 had more intensive phosphate (-63, -79) and potassium (+39) compared to TXD05 (**Fig. S1**). In particular, phosphate intensity was a few times higher than TDX05. On the other hand, TXD05 had higher signals of sodium- and nitrogen-containing compounds as well as stronger amine markers, i.e., m/z +30 (NO/CH_3NH^+) and +58 (C_2H_5-NH-CH_2^+), than TXD01.

A more detailed analysis of the individual mass spectra revealed several distinct particle types. Using a combination of the fuzzy c-means clustering (Shen et al., 2019) and the marker peak search method based on the above-mentioned and other characteristic ions, we found several distinct composition classes, such as "Potassium-rich," “Potassium and phosphate-rich,” “Potassium, sodium, and ammonium rich,” “Amine rich,” and “Mineral and Metal-rich.” We note that the “rich” used here only indicates intensive characteristic peaks in the mass spectra rather than a large mass fraction. **Figure S2** shows the fuzzy classification results. As can be seen, there was no notable size-dependent composition for both sample types. A significant amount of carboxylic acid groups (i.e., m/z -45 and -71) was found in each particle. These prevalent organic markers suggest that, regardless of the classification, TXD are predominantly organic in nature. This organic predominance as well as the substantial inclusion of salts (e.g., potassium) are consistent with our previous study of TXD particles’ composition (Hiranuma et al., 2011). We also note that our LAAPTOF aerosol particle chemical composition analysis was not intended to find ice nucleation (IN) active composition. Ice-nucleating particles (INPs) generally represent a small subset of aerosol particles (roughly one per million, even at low temperatures). Thus, examining aerosol particle chemical composition cannot be directly linked to the role of chemistry in IN. In other words, aerosol particle composition does not necessarily represent INP composition. However, aerosol particle composition data are important for understanding the general chemical compositions of our samples.

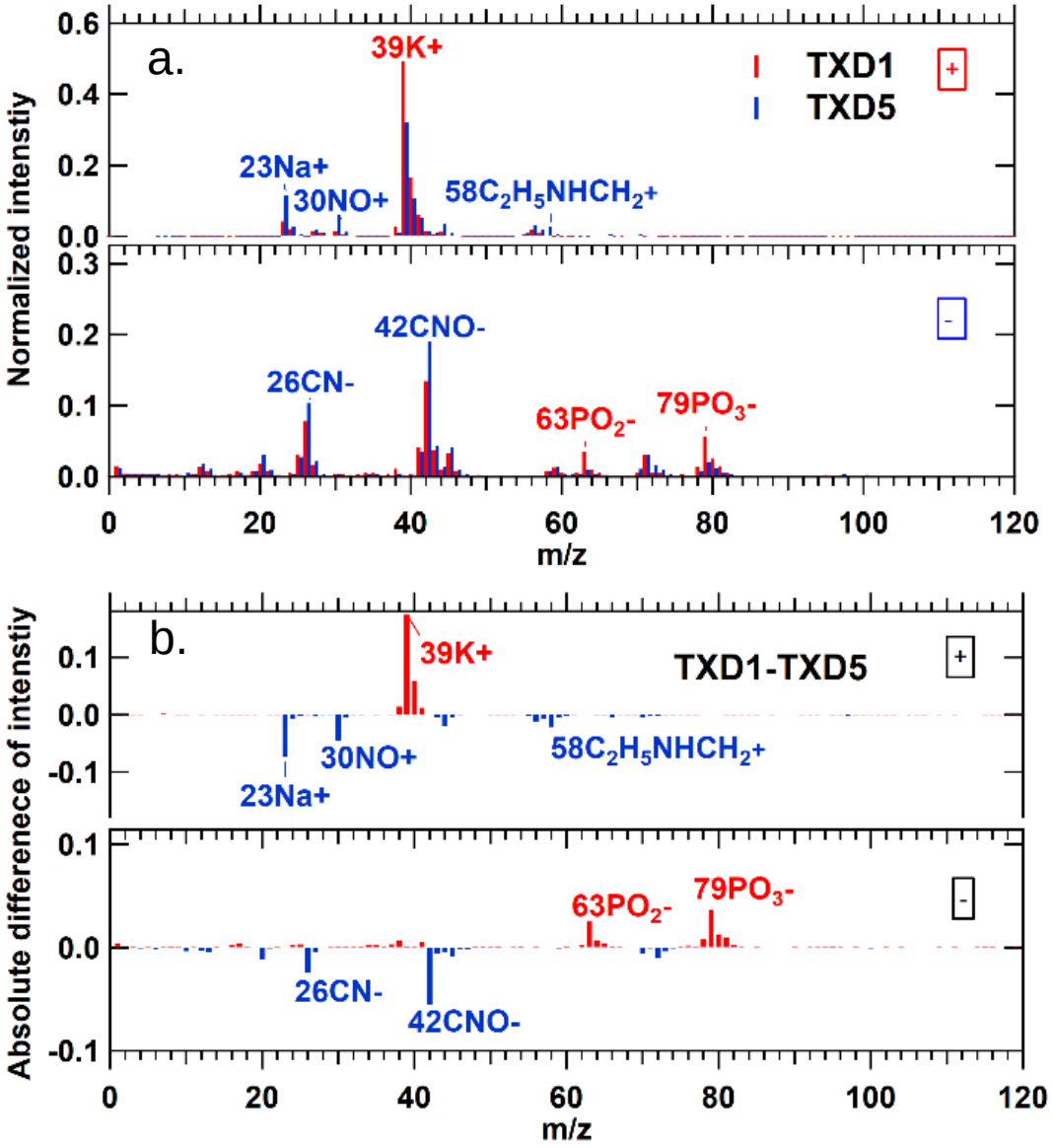

Figure S1. Laboratory reference mass spectra of dry dispersed TXD01 and TXD05 particles with LAAPTOF. (a) The stacked averaged spectra of cations (top) and anions (bottom) found in TXD01 and TXD05. (b) The absolute signal difference. These mass spectra represent a compilation of > 450 of the particles for each type (TXD01: 972 and TXD05: 472). Note that each ion peak intensity is normalized to the sum of ion signals in each spectrum before further compilation.

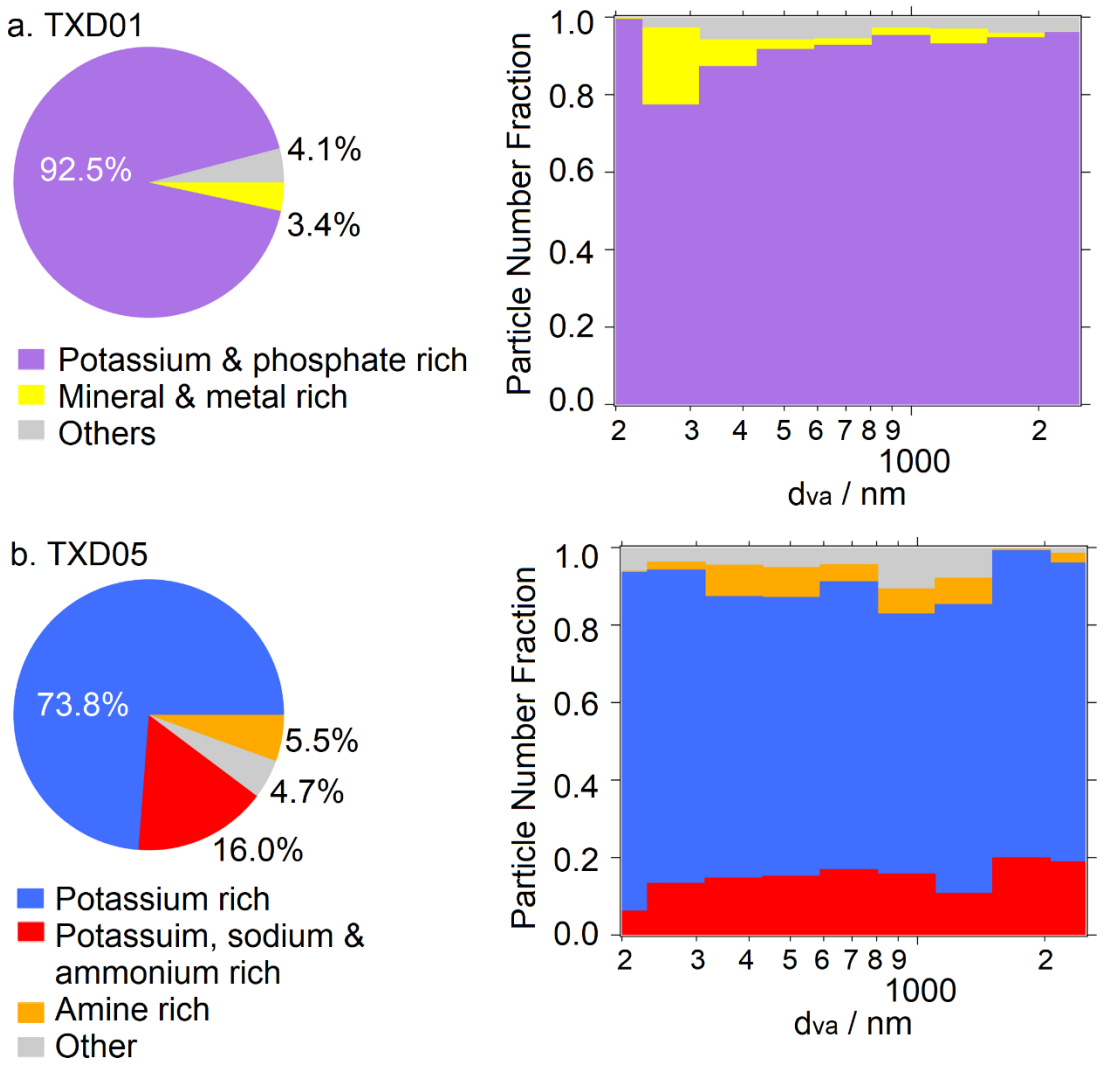

70

Figure S2. Particle population fraction and size distribution based on clustered types, for TXD01 (a) and TXD05 (b). Note that the class named “others” (in grey color) is the small fraction of particles with unknown patterns. This class differs across TXD particle samples.

S2. Taxonomic diversity of two Texas dust samples.

Table S1 summarizes our results of metagenomics analysis. Here we describe the methodology employed for our metagenomics analysis of sample microbiomes.

As the first step of the microbiome analysis, all reads with ambiguous bases ("N") were removed. Chimeric reads were identified and removed based on the de-novo algorithm of UCHIME (Edgar et al., 2011) as implemented in the VSEARCH package (Rognes et al., 2016). The remaining set of high-quality reads was processed using minimum entropy decomposition (MED; Eren et al., 2013 and 2015). MED provides a computationally efficient means to partition marker gene datasets into operational taxonomic units (OTUs). Each OTU represents a distinct cluster with a significant sequence divergent from any other cluster. By employing Shannon entropy, MED uses only the information-rich nucleotide positions across reads and iteratively partitions large datasets while omitting stochastic variation. The MED procedure outperforms classical identity-based clustering algorithms. Sequences can be partitioned based on relevant single nucleotide differences without being susceptible to random sequencing errors. This allows a decomposition of sequence datasets with a single nucleotide resolution. Furthermore, the MED procedure identifies and filters random "noise" in the dataset, i.e., sequences with very low abundance (less than 0.02% of the average sample size).

To assign taxonomic information to each OTU, DC-MEGABLAST alignments of cluster-representative sequences to the sequence database were performed. The most specific taxonomic assignment for each OTU was then transferred from the set of best-matching reference sequences (lowest common taxonomic unit of all the best matches). A sequence identity of 70% across at least 80% of the representative sequence was the minimal requirement for considering reference sequences. Further processing of OTUs and taxonomic assignments were performed using the QIIME software package (version 1.9.1, http://qiime.org/). Abundances of bacterial taxonomic units were normalized using lineage-specific copy numbers of the relevant marker genes to improve estimates. Taxonomic assignments were performed using the NCBI_nt reference database (Release 2019-01-05).

Table S1. An abundance of major orders of *Archaea* (a) Bacteria (b) and Eukaryotes (c) in dust samples TXD01 and TXD05. Numbers indicate the percentage of the OTUs for each order in the total archaeal, bacterial and eukaryotic microbiome. The analysis of the aerosolized TXD01 sample did not generate any useful archaeal data.

a. Archaea Taxonomy	**TXD01**	**TXD05**
Unclassified	-	0.00%
Euryarchaeota; Methanobacteria; Methanobacteriales	-	93.80%
Euryarchaeota; Methanomicrobia; Methanomicrobiales	-	0.10%
Euryarchaeota; Methanomicrobia; Methanosarcinales	-	0.00%
Euryarchaeota; Thermoplasmata; Methanomassiliicoccales	-	0.00%
Thaumarchaeota; Nitrososphaeria; Nitrososphaerales	-	6.10%
b. Bacteria Taxonomy	**TXD01**	**TXD05**
Unclassified	4.00%	2.60%
Actinobacteria; Acidimicrobiales	0.80%	0.20%
Actinobacteria; unclassified	3.00%	2.10%
Actinobacteria; Actinomycetales	0.20%	0.00%
Actinobacteria; Bifidobacteriales	0.00%	0.00%
Actinobacteria; Corynebacteriales	16.40%	13.70%
Actinobacteria; Frankiales	0.20%	0.00%
Actinobacteria; Geodermatophilales	0.30%	0.00%
Actinobacteria; Glycomycetales	0.20%	0.40%
Actinobacteria; Jiangellales	0.00%	0.00%
Actinobacteria; Kineosporiales	0.00%	0.00%
Actinobacteria; Micrococcales	12.30%	2.10%
Actinobacteria; Micromonosporales	0.10%	0.00%
Actinobacteria; Propionibacteriales	5.00%	0.20%
Actinobacteria; Pseudonocardiales	7.70%	39.20%

Actinobacteria; Streptomycetales	11.30%	28.60%
Actinobacteria; Streptosporangiales	2.30%	6.50%
Actinobacteria; Coriobacteriales	0.00%	0.00%
Actinobacteria; Solirubrobacterales	0.20%	0.00%
Bacteroidetes; unclassified	0.10%	0.00%
Bacteroidetes; Chitinophagales	0.30%	0.00%
Bacteroidetes; Cytophagales	0.70%	0.00%
Bacteroidetes; Flavobacteriales	4.20%	0.00%
Bacteroidetes; Saprospirales	0.10%	0.00%
Bacteroidetes; Sphingobacteriales	1.10%	0.00%
Chloroflexi; Sphaerobacterales	4.00%	1.10%
Cyanobacteria; Chroococcales	0.00%	0.00%
Fibrobacteres; Fibrobacterales	0.00%	0.00%
Firmicutes; unclassified	0.10%	0.00%
Firmicutes; Bacilli; unclassified	0.10%	0.00%
Firmicutes; Bacillales	6.10%	2.40%
Firmicutes; Lactobacillales	0.60%	0.00%
Firmicutes; Clostridiales	5.90%	0.30%
Firmicutes; Erysipelotrichales	1.00%	0.10%
Firmicutes; Acidaminococcales	0.00%	0.00%
Firmicutes; Tissierellia; unclassified	0.00%	0.00%
Firmicutes; Tissierellales	0.00%	0.00%
Gemmatimonadetes; Gemmatimonadales	0.40%	0.00%
Gemmatimonadetes; Longimicrobiales	0.00%	0.00%
Nitrospinae; Nitrospinales	0.00%	0.00%
Planctomycetes; Candidatus Brocadiales	0.00%	0.00%
Proteobacteria; unclassified	0.10%	0.00%
Proteobacteria; Alphaproteobacteria; unclassified	0.30%	0.00%
Proteobacteria; Alphaproteobacteria; Caulobacterales	0.50%	0.00%
Proteobacteria; Alphaproteobacteria; Rhizobiales	2.90%	0.00%
Proteobacteria; Alphaproteobacteria; Rhodobacterales	0.50%	0.00%
Proteobacteria; Alphaproteobacteria; Rhodospirillales	0.00%	0.00%
Proteobacteria; Alphaproteobacteria; Sphingomonadales	1.60%	0.00%
Proteobacteria; Betaproteobacteria; Burkholderiales	1.30%	0.00%
Proteobacteria; Deltaproteobacteria; Desulfuromonadales	0.00%	0.00%
Proteobacteria; Deltaproteobacteria; Myxococcales	0.00%	0.00%
Proteobacteria; Gammaproteobacteria; unclassified	0.00%	0.00%
Proteobacteria; Gammaproteobacteria; Aeromonadales	0.00%	0.00%
Proteobacteria; Gammaproteobacteria; Cardiobacteriales	0.00%	0.00%
Proteobacteria; Gammaproteobacteria; Cellvibrionales	0.40%	0.00%
Proteobacteria; Gammaproteobacteria; Chromatiales	0.00%	0.00%
Proteobacteria; Gammaproteobacteria; Enterobacterales	1.60%	0.50%
Proteobacteria; Gammaproteobacteria; Nevskiales	0.00%	0.00%
Proteobacteria; Gammaproteobacteria; Oceanospirillales	0.00%	0.00%
Proteobacteria; Gammaproteobacteria; Pseudomonadales	0.60%	0.00%
Proteobacteria; Gammaproteobacteria; Xanthomonadales	1.00%	0.00%
Proteobacteria; Bdellovibrionales	0.50%	0.00%
Rhodothermaeota; Rhodothermales	0.00%	0.00%
Spirochaetes; Spirochaetales	0.00%	0.00%
c. Eukaryotes Taxonomy	**TXD01**	**TXD05**
Unclassified	0.30%	1.60%
Trichiida	0.00%	0.00%
Oligohymenophorea; Philasterida	0.00%	0.00%
Oligohymenophorea; Sessilida	0.00%	0.00%
Phyllopharyngea; Chlamydodontida	0.00%	0.00%
Spirotrichea; Sporadotrichida	0.00%	0.00%
Ascomycota; unclassified	1.10%	0.90%
Ascomycota; Capnodiales	0.00%	0.00%
Ascomycota; Pleosporales	0.00%	0.00%
Ascomycota; Eurotiales	1.30%	2.80%
Ascomycota; Onygenales	1.70%	5.20%

Ascomycota; Pertusariales	0.00%	0.00%
Ascomycota; Leotiomycetes; unclassified	0.10%	0.00%
Ascomycota; Rhytismatales	0.00%	0.00%
Ascomycota; Thelebolales	0.00%	0.00%
Ascomycota; Pezizales	68.00%	20.40%
Ascomycota; Saccharomycetales	0.10%	0.10%
Ascomycota; Glomerellales	0.00%	0.00%
Ascomycota; Hypocreales	16.90%	59.50%
Ascomycota; Melanosporales	0.10%	0.10%
Ascomycota; Microascales	0.60%	3.10%
Ascomycota; Sordariales	5.30%	2.80%
Basidiomycota; unclassified	0.00%	0.00%
Basidiomycota; Sporidiobolales	0.00%	0.00%
Basidiomycota; Tremellomycetes; unclassified	0.00%	0.00%
Basidiomycota; Trichosporonales	4.40%	3.30%
Basidiomycota; Wallemiales	0.00%	0.00%
Chytridiomycota; Rhizophlyctidales	0.00%	0.00%
Chytridiomycota; Spizellomycetales	0.00%	0.00%
Chytridiomycota; Neocallimastigales	0.00%	0.00%
Mucoromycota; Mortierellales	0.00%	0.00%
Mucoromycota; Mucorales	0.10%	0.20%

S3. Comparison of two immersion freezing techniques

The West Texas cryogenic refrigerator applied to freezing test system (WT-CRAFT) system and the ice nucleation spectrometer of the Karlsruhe Institute of Technology (INSEKT) were compared using an identical sample collected at an open-lot livestock facility (OLLF). This complementary analysis was performed to indirectly validate WT-CRAFT against INSEKT measurements. The data from both techniques were analyzed and compared in terms of ambient INP concentration, n_{INP}. We used the field aerosol particle samples collected using polycarbonate filter samplers at OLLF-3 on July 24th 2019 for this comparison test (**Table 2**). A 50% split of the filter was used for each assay to measure n_{INP} as a function of temperature, $n_{INP}(T)$, by the methods described in **Sects. 2.1.3** (INSEKT) and **2.2.3** (WT-CRAFT). Using this sample for the comparison is reasonable since its n_{INP} spectra fall between the measured maximum and minimum $n_{INP}(T)$ in 2017-2019 even when considering 95% binomial confidence intervals (CI95%). Thus, it is representative of the field OLLF $n_{INP}(T)$ data presented in this study. **Figure S3** shows the $n_{INP}(T)$ spectra of the same sample measured by WT-CRAFT and INSEKT in the temperature range between -8 °C and -22.5 °C. As can be seen, both techniques successfully generated $n_{INP}(T)$ data virtually overlapping within error bars. At temperature < -22°C, WT-CRAFT measures lower values. The two methods correlate well with each other, with the Pearson correlation coefficient (r) of 0.90 ($n_{INP,INSEKT} = (2.12 \times n_{INP,WT\text{-}CRAFT}) - 11.23$).

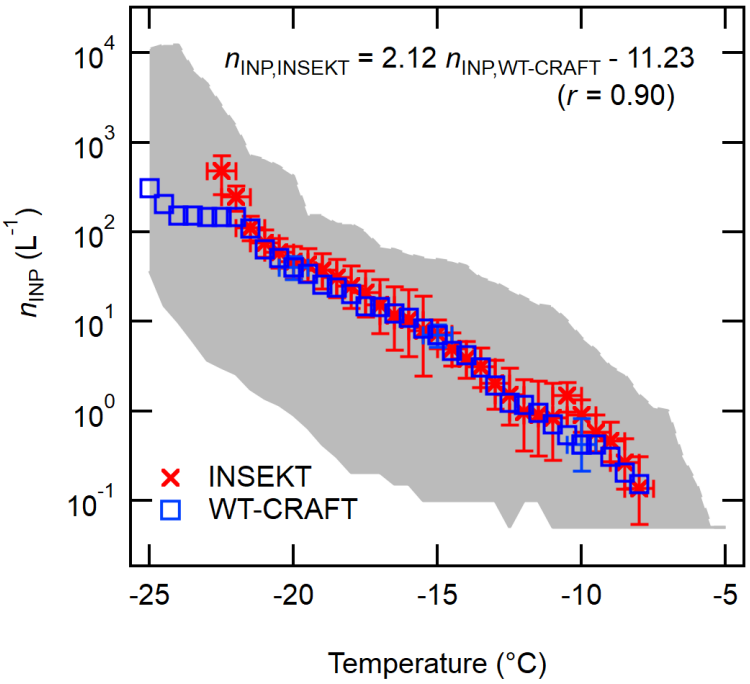

Figure S3. The $n_{INP}(T)$ spectra of aerosol particles collected at OLLF-3 in summer 2019, measured with WT-CRAFT (blue) and INSEKT (red).The uncertainties in temperature and n_{INP} are ± 0.5 °C and ± CI95%, respectively. Error bars are shown at selected temperatures for the WT-CRAFT data to make all data points visible. The shaded area represents max – min $n_{INP}(T)$ for all our OLLF samples collected in 2017 – 2019.

S4. Heat treatment analysis

INSEKT was also used to assess immersion freezing ability and efficiency of heated filter samples. As explained in **Sect. 2.1.3**, a series of diluted samples were examined in INSEKT. We made sure to assess overlapping *T* intervals in a series of measurements to see if immersion freezing spectra from multiple measurements agree within CI95%.

As for heat treatment, the suspension sample tube was immersed in boiling water (~100 °C) for 20 minutes. This temperature was chosen to denature proteinaceous INPs. The choice of 100 °C for heat treatment seems valid because proteinaceous structures will be destroyed below ~ 100 °C (Steinke et al., 2016). For example, Szyrmer and Zawadzki (1997) found some known cell-free IN-active microbes (e.g., *Fusarium* nuclei) are stable only up to 60 °C. Other than this study, IN activity by bacteria (Morris et al., 2004; Christner et al., 2008), fungi (Humphreys et al., 2001), and lichens (Henderson-Begg, et al., 2009) has been shown to be heat-sensitive irreversibly at 100 °C or below. Other soil organic components can be decomposed at temperatures between 100 °C and 300 °C (Tobo et al., 2014). Thus, subtracting heated n_{INP} or INP concentration per unit geometric particle surface area ($n_{s,geo}$) from non-heated values allows us to assess their contribution to immersion freezing. The rest of the heating procedure is adapted from Schiebel (2017). Briefly, the aerosol particle suspension (3 mL) from a non-treated stock was first transferred to a sterile falcon tube. The screw-cap was closed, such that no water was lost. Then the tube was placed together with a precisely fitting styrofoam ring in a water-filled glass beaker. The styrofoam ring ensured that the tube was floating, and all of the aerosol suspension was submerged below the water surface for best heat transfer. The beaker was placed on a stirring hot plate to boil the water.

The effect of heat treatment on our laboratory and field samples for immersion freezing, summarized in **Fig. S4**, revealed inclusion of heat-labile INPs in our laboratory samples but not in the field sample. While the effect of heat treatment is not as obvious as what was previously observed in other soil dust samples: e.g., a wheat harvest soil dust in Suski et al. (2018), the TXD01 sample showed a reduction in $n_{s,geo}$ at temperatures above -22 °C after heat treatment. At -19 °C, the heat eliminated INPs for our detection limit in this study (i.e., $n_{s,geo} \approx 5 \times 10^5$ m^{-2}). Similarly, TXD05 also exhibited a sensitivity to heat above -20 °C. Heating reduced the freezing efficiency of the TXD05 sample below our detection limit at -19 °C. From our metagenomics analysis, presented in **Sect. 3.1.4**, no known IN-active microbiomes are present in our laboratory samples, which limits the heat-labile composition to be heat sensitive organics.

In contrast, heat treatment on the field sample, collected in OLLF-3 on July 24th, 2019, did not show substantial sensitivity to heat compared to our laboratory samples. The INP concentrations are reduced in the temperature range between -10 °C and -12.5 °C, presumably due to the loss of heat-labile INPs. However, the overall heat-stable feature of this field sample suggests the presence of immersion freezing mode active heat-stable components, including non-heat-labile organics and mineral compounds. This heat-resistant feature of OLLF samples may also be due to their pre-exposure to soil temperature on average higher than ambient temperature even at a depth of 150 mm during summer (Cole et al., 2009).

Previously, Suski et al. (2018) found that heat-treatment (95 °C for 20 min) can suppress the n_{INP} of wheat harvest soil dust samples from Kansas, USA by more than two orders of magnitude at -12 °C. The authors concluded that the decomposition of IN-active heat-labile organics and bacteria is responsible for the observed n_{INP} suppression. This result is consistent with the impact of heat treatment on the IN efficiency of soil dust samples from different regions, such as the one from a lodgepole pine forest in Wyoming, USA (Hill et al., 2016; 105 °C for 20 min) and another from Central Yakutia (Conen et al., 2011; 100 °C for 10 min). Similarly, Tobo et al. (2014) found that 300 °C combustion can reduce the IN fraction of Wyoming soil dust at -24 °C by the same orders of magnitude observed by Suski et al. (2018). In contrast, Steinke et al (2016) found no notable effect of heat treatment (~ 110 °C) on the Argentinian soil dust IN efficiency at ~ -24 °C. This heat-stable nature of Argentinian soil dust may have coincided with its lack of IN-active proteins and/or heat-sensitive microbes, which aligns with the absence of known IN-active microbes in our OLLF samples. In total, our findings and the observations by Steinke et al. (2016) eliminate proteinaceous and biological ice-nucleating components as the primary source of IN

abundance in air. Thus, the investigation of heat-stable organic INPs is key to further understand the properties of soil dust INPs. Future research should focus on understanding how organic composition influences atmospheric immersion freezing. Our current knowledge regarding IN-active organics is still limited.

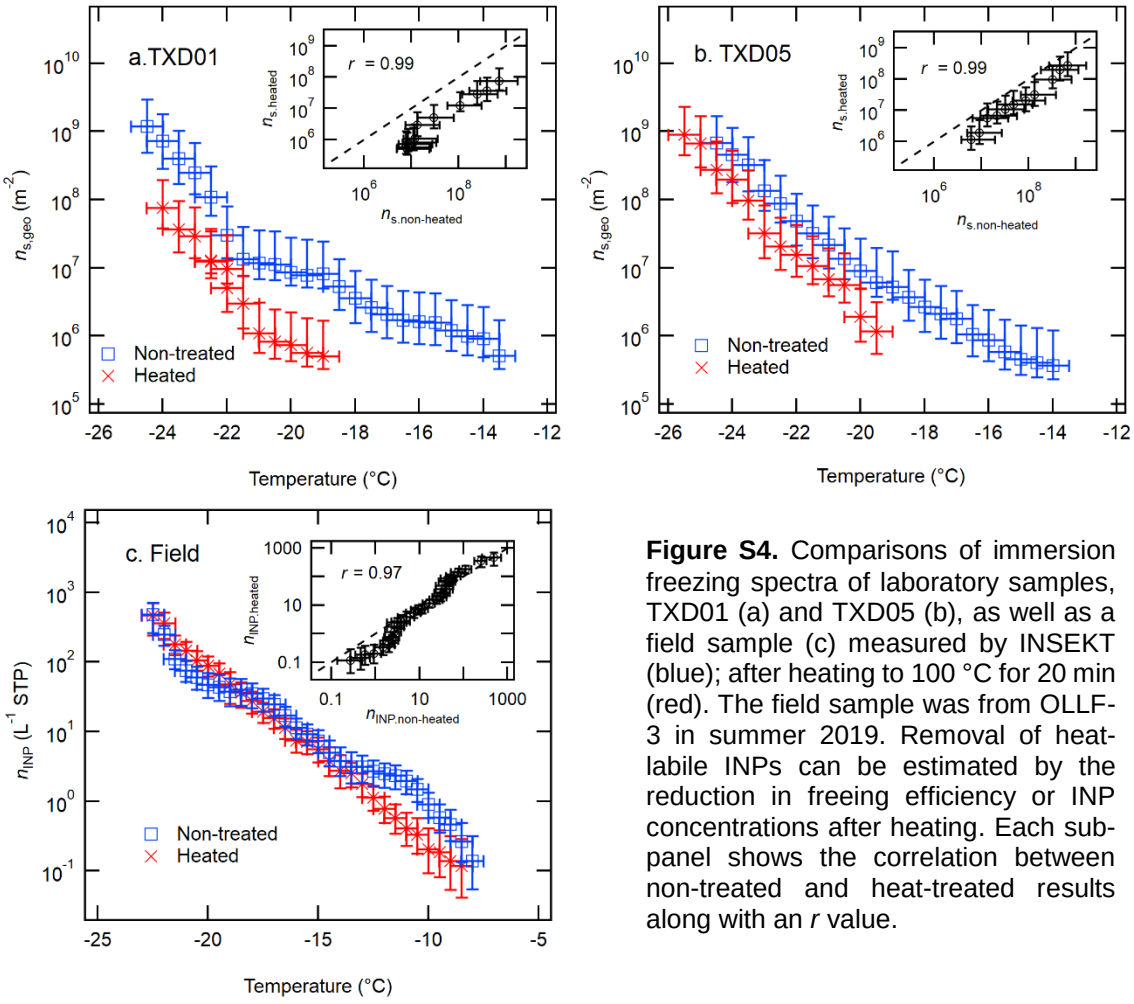

Figure S4. Comparisons of immersion freezing spectra of laboratory samples, TXD01 (a) and TXD05 (b), as well as a field sample (c) measured by INSEKT (blue); after heating to 100 °C for 20 min (red). The field sample was from OLLF-3 in summer 2019. Removal of heat-labile INPs can be estimated by the reduction in freeing efficiency or INP concentrations after heating. Each sub-panel shows the correlation between non-treated and heat-treated results along with an *r* value.

S5. Estimated INPs released from an OLLF

Tapered-element oscillating microbalances (TEOMs; Thermo Scientific Inc., Model 1400ab; Patashnick and Rupprecht, 1991) were deployed at OLLF-1 to continuously monitor mass concentrations of particulate matter less than 10 μm diameter (PM_{10}). Two identical TEOMs were deployed at OLLF-1: one at the upwind edge and another at the downwind location of OLLF-1 (**Fig. 2**). With an operating flow rate of 16.7 LPM, our TEOM measured < 1 g m^{-3} of PM with a 5-min time resolution. Both TEOMs ran continuously during the entire 2016 – 2019 study period except for routine maintenance activities. The inlets of DustTrak and TEOMs were maintained at ~ 1.5 m above the ground to be consistent with our polycarbonate filter samplers. It is noteworthy that our TEOM and DustTrak PM_{10} measurements agreed within ± 40% on average.

To complement our observation, we estimated ambient INP concentration at OLLF-1 based on our field mass concentration data, using the OLLF-1 TEOM PM_{10} data. We chose to use the OLLF-1 data due to their reasonable spatiotemporal coverage (i.e., two identical model TEOMs deployed at the downwind and upwind sites for 2016 – 2019). A summary of TEOM mass concentration data in different seasons over 2016 – 2019 is available in **Table S2**. In general, PM_{10} mass concentrations from OLLF-1 (average ± standard errors) were high in meteorological summers ($3.9 \times 10^{-7} \pm 5.6 \times 10^{-8}$ g L^{-1}) and springs ($4.5 \times 10^{-7} \pm 2.4 \times 10^{-7}$ g L^{-1}) as compared to fall ($2.4 \times 10^{-7} \pm 4.4 \times 10^{-8}$ g L^{-1}) and winter ($1.5 \times 10^{-7} \pm 5.3 \times 10^{-8}$ g L^{-1}). A similar trend was found for the upwind PM_{10} mass concentration: summer ($3.4 \times 10^{-8} \pm 9.0 \times 10^{-9}$ g L^{-1}) ≥ spring ($2.8 \times 10^{-8} \pm 9.3 \times 10^{-9}$ g L^{-1}) > fall ($1.8 \times 10^{-8} \pm 5.7 \times 10^{-9}$ g L^{-1}) ≥ winter ($1.4 \times 10^{-8} \pm 7.1 \times 10^{-10}$ g L^{-1}). But, the measured values at the upwind location are consistently an order magnitude lower than that from the downwind location.

Frequently, the observed PM_{10} concentration exceeded 10^{-7} g L^{-1}, which is consistent with previous studies (Bush et al., 2014). On the other hand, the observed mass concentration at the upwind sites was lower except for known/recorded interruptions (e.g., a tractor-trailer passing by), resulting in a transient increase in mass concentration. As the upwind n_{INP} can be considered non-negligible (see **Sect. 3.2.1**), we subtracted mass concentrations measured at a nominal upwind edge from the downwind TEOM mass concentration values to compute PM_{10} from OLLF-1. The screened TEOM data were used as ambient particle concentration data to estimate n_{INP} from an OLLF.

Due to the atmospheric relevance and temperature coverage extending to -5 °C, we used a fit of ***Field_Median*** in **Table S3** to compute representative $n_{s,geo}$ relevant to OLLF. To convert $n_{s,geo}$ to n_{INP}, we have adapted Equations (1) – (3) in **Sect. 2.1.3**. Briefly, the measured mass concentration, as well as field specific surface area (SSA), were used to convert from $n_{s,geo}$ to n_{INP}:

$$n_{INP}(T)(L^{-1}) = n_{s,geo}(T)(m^{-2}) \times Geometric\ SSA\ \left(\frac{m^2}{g}\right) \times \text{Mass Conc.}\left(\frac{g}{L}\right). \qquad [S1]$$

where the geometric *SSA* value for field data is ~ 0.4 m^2 g^{-1} (**Sect. 2.2.3**). Our assumption of n_{INP} to be linearly scaled to mass concentration is supported by the observed correlation between PM mass and n_{INP} (**Fig. 7a**).

Table S2 also summarizes the TEOM estimated annual and seasonal n_{INP} from 2016 to 2019. On average, the estimated mean n_{INP} values at -15, -20, and -25 °C in 2016 – 2019 were estimated as 46.8 (±25.3 seasonal standard deviation; same hereafter), 288.1 (± 156.1), and 5,250.9 (± 2,845.6) L^{-1}, respectively. In addition, the median n_{INP} at -15, -20, and -25 °C in 2016 – 2019 were estimated as 14.7 (± 9.2), 90.9 (± 56.4), and 1,656.3 (± 1,028.1) L^{-1}, respectively. As our n_{INP} is linearly scaled to mass concentration (Eqn. S1), estimated n_{INP} showed a similar seasonal variability as seen in mass concentration. For instance, at -20 °C, the cumulative n_{INP} averages for each meteorological season over three years from 2016 to 2019 were estimated as follows: spring (315.4 ± 164.9 L^{-1}) ≥ summer (270.4 ± 39.0 L^{-1}) > fall (165.1 ± 30.8 L^{-1}) ≥ winter (106.9 ± 36.8 L^{-1}). The observed high n_{INP} values were expected for such high PM_{10} mass concentrations emitted from the cattle feedlot, which represent an important point source of agricultural aerosol particle emission. However, we reemphasize that the IN efficiency of OLLF aerosol particles is similar to other agricultural aerosol particles found in previous studies as shown in **Fig. 4**.

Figure S5 displays the TEOM mass concentration time series over 2016 – 2019 as well as cumulative n_{INP} estimated at temperatures of -15 °C, -20 °C, and -25 °C. The background mass concentration measured at the upwind location (1.7×10^{-8} to 2.6×10^{-8} g L^{-1}) is shown with a red dashed line in **Fig. S5a** and subtracted from the downwind data. The resulting OLLF mass concentration was on average $4.12 \times 10^{-7} \pm 2.96 \times 10^{-9}$ g L^{-1} (or 411.57 ± 2.96 μg m^{-3}). Annual averages of OLLF mass concentrations are indicated with a blue dashed line in **Fig. S5a**. On average, the downwind concentration exhibited higher mass concentration by more than an order of magnitude. This result implies a constant high particle load from the OLLF, which was also seen by a previous study at the same OLLF (Hiranuma et al., 2011). Seasonal variation is also seen in **Fig. S5a,** as the annual peak of mass concentration (> 10^{-5} g L^{-1}) coincided with summer in each case.

Figure S5b shows associated n_{INP} estimations. The average estimated INPs at three different temperatures, -15 °C, -20 °C, and -25 °C, are shown as a gray dashed line, black dashed line, and black solid line, respectively. Our results show that the aerosol particles downwind of a feedlot contain several thousand INPs L^{-1} (median = 1,656 L^{-1}; average = 5,251 L^{-1}) at standard temperature and pressure (STP) at -25 °C, which is three orders of magnitude higher than typical ambient n_{INP} from continental sources as reported in DeMott et al. (2010). More discussion of OLLF n_{INP} in comparison with previous studies is provided in **Sect. 3.2.3**. We note that our estimation of n_{INP} is limited at the source location. Further understanding of OLLF-derived INPs in the atmosphere will require future research in the dust generation mechanisms in association with local dynamics and thermodynamics, vertical distribution of OLLF dust, and their fate in the atmosphere.

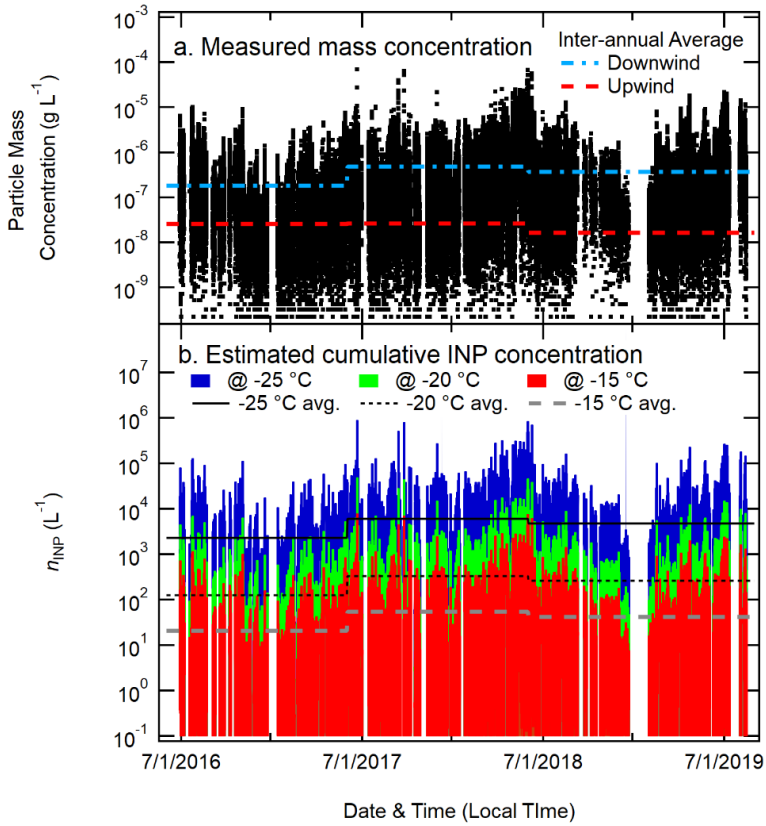

Figure S5. OLLF INP concentrations. Time-series plot of TEOM mass concentration measured at the downwind side of OLLF-1 (a) and cumulative n_{INP} estimated at temperatures of -15 °C, -20 °C, and -25 °C (b). In Panel a, inter-annual average mass concentrations of aerosol particles from OLLF (blue dashed line) and upwind (red dashed line) are shown (numbers adapted from **Table S2**). In Panel b, likewise, inter-annual average n_{INP} estimated at -15, -20, and -25 °C (reported in **Table S2**) are also shown. Meteorological summer in Texas is used for the beginning and ending timestamps of each year.

Table S2. Inter-annual and seasonal PM_{10} mass concentrations from OLLF-1 as well as estimated n_{INP}.

	PM_{10} Mass Concentration (g L^{-1})		Estimated $n_{INP}(T)$ (L^{-1})		
	*OLLF	Upwind	T = -15 °C	T = -20 °C	T = -25 °C
2016 – 2017	**1.8E-07**	**2.6E-08**	**20.7**	**127.5**	**2323.4**
Summer	3.7E-07	5.2E-08	42.3	260.5	4747.7
Fall	1.6E-07	2.8E-08	18.1	111.7	2036.3
Winter	6.3E-08	1.5E-08	7.2	44.2	806.2
Spring	1.6E-07	2.1E-08	17.7	108.9	1985.5
2017 – 2018	**4.8E-07**	**2.6E-08**	**54.6**	**336.4**	**6133.0**
Summer	3.0E-07	2.3E-08	33.8	208.5	3801.1
Fall	3.1E-07	1.9E-08	35.4	218.2	3978.3
Winter	2.5E-07	1.3E-08	27.9	171.7	3129.6
Spring	9.2E-07	4.6E-08	104.1	641.3	11690.9
2018 – 2019	**3.7E-07**	**1.7E-08**	**42.3**	**260.7**	**4752.5**
Summer	4.9E-07	2.6E-08	55.6	342.3	6240.6
Fall	2.4E-07	7.9E-09	26.8	165.3	3013.0
Winter	1.5E-07	1.3E-08	17.0	104.8	1910.2
Spring	2.8E-07	1.6E-08	31.8	195.8	3570.0

*Upwind concentration is subtracted.

Table S3. OLLF-INP parameterization: List of exponential fit parameters to the $n_{s,geo}$ for temperature-binned ensemble datasets of lab study as well as field study. The datasets are fitted in the log space. The *r* value for each fit is also shown. All $n_{s,geo}$ values are in m^{-2}. temperature is in °C. Note the fifth-order polynomial fit function is sensitive for all decimals shown here. To reproduce the fitted curves, we needed to include all decimals.

Fitted dataset: Sample ID (INSEKT sample type)	Fitted *T* range	Fit Parameters $n_{s,geo}(T) = \exp(a + b \cdot T + c \cdot T^2 + d \cdot T^3 + e \cdot T^4 + f \cdot T^5]$							
		a (m^{-2})	*b* (m^{-2} °C^{-1})	*c* (m^{-2} °C^{-2})	*d* (m^{-2} °C^{-3})	*e* (m^{-2} °C^{-4})	*f* (m^{-2} °C^{-5})	*r*	Δlog ($n_{s,geo}$)/Δ*T*
TXD01 (filter)	-29˚C < *T* < -13.5˚C	-649.60926 6142404	-166.17848 0154537	-16.33142 45417013	-0.78540 3143752226	-0.01845 63650678816	-0.00017 023048008878	0.99	0.41
TXD05 (filter)	-28.5˚C < *T* < -14˚C	-313.30582 52180446	-75.91269 8717769	-6.90433 259329411	-0.30470 8262752833	-0.00646 068282529837	-5.27553 644987649e-05	0.62	0.42
Field_ Median	-25˚C < *T* < -5˚C	-29.64701 0567958	-16.31705 83864393	-2.30949 598965458	-0.16257 04680712	-0.00552 393352312353	-7.23939 690197926e-05	0.94	0.52

S6. List of abbreviations

- AIDA: aerosol interaction and dynamics in the atmosphere
- APS: aerosol particle sizer
- BET: Brunauer-Emmett-Teller
- CI95%: 95% confidence intervals
- $C_{INP}(T)$: nucleus concentration in ultrapure water suspension
- CPC: condensation particle counter
- DF: dilution factor
- DFPC: dynamic filter processing chamber
- D_{ve}: volume equivalent diameter
- $f_{unfrozen}(T)$: ratio of the number of droplets unfrozen to the total number of droplets
- ICR: ice crystal residual
- IN: ice nucleation
- INP: ice-nucleating particle
- INSEKT: IN spectrometer of the Karlsruhe Institute of Technology
- LAAPTOF: laser ablation aerosol particle time-of-flight mass spectrometer
- MED: minimum entropy decomposition
- M_{ve}: mass of a spherical particle of volume equivalent diameter
- $n_{INP}(T)$: INP concentration per unit standard air volume as a function of temperature
- $n_m(T)$: INP concentration per unit particle mass as a function of temperature
- $n_{s,geo}(T)$: INP concentration per unit geometric particle surface area as a function of temperature
- O14: O'Sullivan *et al*. (2014)
- OLLF: open-lot livestock facility
- OTU: operational taxonomic unit
- PFS: polycarbonate filter sampler
- PM: particulate matter
- PM_x = particulate matter smaller than x μm in diameter
- *r*: correlation coefficient
- *RH*: relative humidity
- S16: Steinke *et al*. (2016)
- S20: Steinke et al. (2020)
- SI: Supplemental Information
- SMPS: scanning mobility particle sizer
- *SSA*: specific surface area
- S_{total}/M_{total}: geometric specific surface area
- STP: standard temperature and pressure
- Su18: Suski et al. (2018)
- T14: Tobo et al. (2014)
- TEOM: tapered-element oscillating microbalance
- U17: Ullrich *et al*. (2017)
- V_{air}: sampled air volume
- V_d: volume of the sample in a well
- V_l: suspension liquid volume
- WT-CRAFT: West Texas cryogenic refrigerator applied to freezing test system

SI References

S. Angelino et al., Formation of aerosol particles from reactions of secondary and tertiary alkylamines: Characterization by aerosol time-of-flight mass spectrometry. *Environ. Sci. Technol*. **35**, 3130–3138 (2001).

J. Bush et al., Increasing stocking density reduces emissions of fugitive dust from cattle feedyards. *Applied Engineering in Agriculture* **30**, 815–824 (2014).

B. C. Christner et al., Ubiquity of biological ice nucleators in snowfall. *Science* **319**, 1214, https://doi.org/10.1126/science.1149757 (2008).

N. A. Cole et al., Chemical composition of pen surface layers of beef cattle feedyards. *Professional Animal Scientist* **25**, 541–552 (2009).

F. Conen et al., Biological residues define the ice nucleation properties of soil dust. *Atmos. Chem. Phys*. **11**, 9643–9648 (2011).

P. J. DeMott et al., Predicting global atmospheric ice nuclei distributions and their impacts on climate. *Proc. Natl. Acad. Sci. U.S.A.* **107,** 11217–11222 (2010).

R. C. Edgar et al., UCHIME improves sensitivity and speed of chimera detection. *Bioinformatics* **27**, 2194–2200 (2011).

A. M. Eren et al., Oligotyping: differentiating between closely related microbial taxa using 16s rRNA gene data. *Methods, Ecol. Evol*. **4**, 1111–1119 (2013).

A. M. Eren et al., Minimum entropy decomposition: Unsupervised oligotyping for sensitive partitioning of high-throughput marker gene sequences. *The ISME Journal* **9**, 968–979 (2015).

S. K. Henderson-Begg et al., Terrestrial and airborne non-bacterial ice nuclei. *Atmosph. Sci. Lett*. **10**, 215–219 (2009).

T. C. J. Hill et al., Sources of organic ice nucleating particles in soils. *Atmos. Chem. Phys*. **16**, 7195–7211 (2016).

N. Hiranuma et al., High concentrations of coarse particles emitted from a cattle feeding operation. *Atmos. Chem. Phys.* **11**, 8809–8823 (2011).

T. L. Humphreys et al., Sensitivity of Partially Purified Ice Nucleation Activity of Fusarium acuminatum SRSF 616. *Curr. Microbiol*. **42**, 330–338 (2001).

C. E. Morris et al., Ice nucleation active bacteria and their potential role in precipitation. *J. Phys. IV France* **121**, 87–103 (2004).

D. M. Murphy et al., Single-particle mass spectrometry of tropospheric aerosol particles. *J. Geophys. Res.-Atmos*. **111**, D23S32, https://doi.org/10.1029/2006JD007340 (2006).

National Research Council, “Minerals” in *Nutrient Requirements of Beef Cattle: Seventh Revised Edition: Update 2000* (The National Academies Press). pp. 54–69 (2000).

R. Ocsay et al., Characterization and diurnal variation of size-resolved inorganic water soluble ions at a rural background site. *J. Environ. Monitor.* **8**, 300–306 (2006).

D. O'Sullivan et al., Ice nucleation by fertile soil dusts: relative importance of mineral and biogenic components. *Atmos. Chem. Phys*. **14**, 1853–1867 (2014).

H. Patashnick, and E. G. Rupprecht, Continuous PM-10 measurements using the tapered element oscillating microbalance. *Journal of the Air and Waste Management Association* **41**, 1079–1083 (1991).

K. A. Pratt et al., Seasonal volatility dependence of ambient particle phase amines. *Environ. Sci. Technol*. **43**, 5276–5281 (2009).

T. Rognes et al., VSEARCH: a versatile open source tool for metagenomics. *Peer J*. **4**, e2584, https://doi.org/10.7717/peerj.2584 (2016).

T. Schiebel, Ice nucleation activity of soil dust aerosols. Thesis, Karlsruhe Institute of Technology, 131 pp., https://doi.org/10.5445/IR/1000076327 (20 October 2017).

S. Schmidt et al., Online single particle analysis of ice particle residuals from mountain-top mixed-phase clouds using laboratory derived particle type assignment. *Atmos. Chem. Phys.* **17**, 575–594 (2017).

J. Schneider et al., Mass-spectrometric identification of primary biological particle markers and application to pristine submicron aerosol measurements in Amazonia. *Atmos. Chem. Phys.* **11**, 11415–11429 (2011).

X. Shen et al., Laser ablation aerosol particle time-of-flight mass spectrometer (LAAPTOF): Performance, reference spectra and classification of atmospheric samples. *Atmos. Meas. Tech*. **11**, 2325–2343 (2018).
X. Shen et al., Understanding of atmospheric aerosol particles with improved particle identification and quantification by single particle mass spectrometry. *Atmos. Meas. Tech*. **12**, 2219–2240 (2019).
P. J. Silva et al., Single particle analysis of suspended soil dust from Southern California. *Atmos. Environ*. **34**, 1811–1820 (2000).
I. Steinke et al., Ice nucleation activity of agricultural soil dust aerosols from Mongolia, Argentina, and Germany. *J. Geophys. Res.-Atmos*. **121**, 13559–13576 (2016).
I. Steinke et al., Complex plant-derived organic aerosol as ice-nucleating particles – more than the sums of their parts? *Atmos. Chem. Phys.* **20**, 11387–11397 (2020).
K. J. Suski et al., Agricultural harvesting emissions of ice-nucleating particles. *Atmos. Chem. Phys*. **18**, 13755–13771 (2018).
W. Szyrmer, and I. Zawadzki, Biogenic and anthropogenic sources of ice-forming nuclei: A review. *Bull. Am. Meteorol. Soc*. **78**, 209–228 (1997).
Y. Tobo et al., Organic matter matters for ice nuclei of agricultural soil origin. *Atmos. Chem. Phys*. **14**, 8521–8531 (2014).
R. Ullrich et al., A new icenucleation active site parameterization for desert dust and soot. *J. Atmos. Sci*. **74**, 699–717 (2017).
M. A. Zawadowicz et al., Improved identification of primary biological aerosol particles using single particle mass spectrometry. *Atmos. Chem. Phys*. **17**, 7193–7212 (2017).